Available online at www.sciencedirect.com
ScienceDirect
Comput. Methods Appl. Mech. Engrg. 282 (2014) 218–238
Computer methods in applied mechanics and engineering
www.elsevier.com/locate/cma

Bayesian uncertainty quantification and propagation for discrete element simulations of granular materials

P.E. Hadjidoukas[a], P. Angelikopoulos[a], D. Rossinelli[a], D. Alexeev[a], C. Papadimitriou[b], P. Koumoutsakos[a,*]

[a] *Computational Science and Engineering Laboratory, ETH Zürich, CH-8092, Switzerland*
[b] *Department of Mechanical Engineering, University of Thessaly, Pedion Areos, GR-38334 Volos, Greece*

Received 31 January 2014; received in revised form 30 June 2014; accepted 18 July 2014
Available online 11 August 2014

Abstract

Predictions in the behavior of granular materials using Discrete Element Methods (DEM) hinge on the employed interaction potentials. Here we introduce a data driven, Bayesian framework to quantify DEM predictions. Our approach relies on experimentally measured coefficients of restitution for single steel particle–wall collisions. The calibration data entail both tangential and normal coefficients of restitution, for varying impact angles and speeds of the bouncing particle. The parametric uncertainty in multiple Force–Displacement models is estimated using an enhanced Transitional Markov Chain Monte Carlo implemented efficiently on parallel computer architectures. In turn, the parametric model uncertainties are propagated to predict Quantities of Interest (QoI) for two testbed applications: silo discharge and vibration induced mass-segregation. This work demonstrates that the classical way of calibrating DEM potentials, through parameter optimization, is insufficient and it fails to provide robust predictions. The present Bayesian framework provides robust predictions for the behavior of granular materials using DEM simulations. Most importantly the results demonstrate the importance of including parametric and modeling uncertainties in the potentials employed in Discrete Element Methods.

Keywords: Uncertainty quantification; Bayesian model selection; Discrete Element Method; Contact force models; Granular flow

1. Introduction

The Discrete Element Method (DEM) [1] is a powerful technique for simulating particle models of engineering systems. It is the main tool of computational investigation in engineering applications [2] including Silo discharge [3–6], wave propagation through granular media [7], particle mixing on grates and in drums [8–10], fluidized beds [11,12] and plug flows [13].

* Correspondence to: Computational Science and Engineering Laboratory, ETH Zürich, Clausiusstrasse 33, CH-8092, Switzerland. Tel.: +41 44 632 52 58; fax: +41 44 632 17 03.
E-mail address: petros@ethz.ch (P. Koumoutsakos).

http://dx.doi.org/10.1016/j.cma.2014.07.017
0045-7825/

The core of DEM is the selected Force–Displacement (F–D) model that updates the rotational and translational movement for each particle following pairwise collisions with other particles and obstacles. The F–D model reflects the nature of the material and is a low order model of the detailed viscoelastic interactions of each particle with its environment. However F–D models are semi-empirical and often contain several parameters to be identified. The sensitivity of various Quantities of Interest (QoIs) in DEM simulations to the F–D model parameters has been the subject of several investigations [5,14–17]. The common practice is that DEM parameters are calibrated using experimental measurements, without taking into account the experimental and model uncertainty. The search for an optimal DEM model has led to extensive comparative studies [18,19] of different models and parameters. The studies reported in [19] demonstrated the difficulty in defining and asserting the superiority of one model over the others.

Here we investigate the parameters and structure of F–D models in DEM using a Bayesian framework [20–26]. A probabilistic Bayesian Uncertainty Quantification and Propagation (UQ+P) framework is used to quantify and calibrate parameter uncertainties in DEM simulations based on available experimental measurements from system components. Furthermore we propagate these uncertainties in DEM simulations to make robust predictions for relevant QoI.

We focus on evaluating the quantitative predictions of three different F–D models using experimental data for normal and tangential restitution coefficients. The uncertainty in the parameters of these models is estimated, and the most probable model is identified. In turn we propagate uncertainties to QoI in simulations of applications such as Silo Discharge blocking and the "Brazil Nut" effect [27]. We employ an enhanced parallel variant of the Transitional Markov Chain Monte Carlo (TMCMC) algorithm [28,29] along with a parallel framework to distribute the large number of system runs in clusters with heterogeneous computer architectures [30]. Our results help demonstrate the value of the Bayesian framework for DEM simulations and provide credible intervals for their predictions.

The paper is organized as follows: In Section 2 we outline the elements of DEM simulations and in particular the parametric F–D models. Section 3 presents the Bayesian framework and in Section 4 we give the results for the Bayesian Calibration of the F–D model parameters. Section 5 showcases two UQ+P studies on relevant industrial applications using the calibrated uncertainty models from Section 4. Our summary and conclusions are presented in Section 6.

2. The DEM and its implementation

The DEM is a widely used method to simulate granular material with a broad range of industrial applications ranging from oil and gas to pharmaceutical and metallurgy. The granular material is modeled as a set of particles of various shapes with translational and rotational degrees of freedom accompanied by models of interparticle collisions. Each particle has its own mass, velocity and contact properties. The contact forces between particles consist of elastic, viscous and frictional resistance forces.

In this work we consider two-dimensional systems. Two disks with radii R_i, R_j are assumed to be in mechanical contact if $\xi_{ij} \equiv R_i + R_j - \left|\mathbf{r}_i - \mathbf{r}_j\right| > 0$. Here $\mathbf{r}_i - \mathbf{r}_j = \mathbf{r}_{ij}$ is the vector connecting the center of particle i to the center of particle j and ξ_{ij} is the mutual compression between the particles (see Fig. 1). The force exerted on particle i due to contact with particle j is given as $\mathbf{F}_{ij} = \mathbf{F}^n_{ij} + \mathbf{F}^t_{ij}$ where $\left(F^t\right)$ and (F^n) are its tangential and normal contributions (see 1). Following the notation of [31] the normal and the tangential contact force components can be written as

$$\mathbf{F}^n_{ij} = F^n_{ij}\mathbf{e}^n_{ij}, \quad \mathbf{F}^t_{ij} = F^t_{ij}\mathbf{e}^t_{ij} \tag{1}$$

with the unit vectors

$$\mathbf{e}^n_{ij} = \frac{r_j - r_i}{\left|r_j - r_i\right|}, \qquad \mathbf{e}^t_{ij} = \begin{pmatrix} 0 & -1 \\ 1 & 0 \end{pmatrix} \cdot \mathbf{e}^n_{ij}.$$

Particles evolve according to the two-dimensional Newton's equations of motion (2):

$$\begin{aligned} m_i\ddot{\mathbf{r}}_i &= m_i\mathbf{g} + \sum_{j,j\neq i}^{N} \mathbf{F}_{ij}, \qquad I_i\ddot{\phi}_i = \sum_{j,j\neq i}^{N} \left(\mathbf{l}_{ij} \times \mathbf{F}_{ij}\right) \cdot \mathbf{e}^z_{ij} \\ \mathbf{r}_i &= \mathbf{r}_{i0}, \quad \dot{\mathbf{r}}_i = 0, \qquad \phi_i = 0, \quad \dot{\phi}_i = 0 \end{aligned} \tag{2}$$

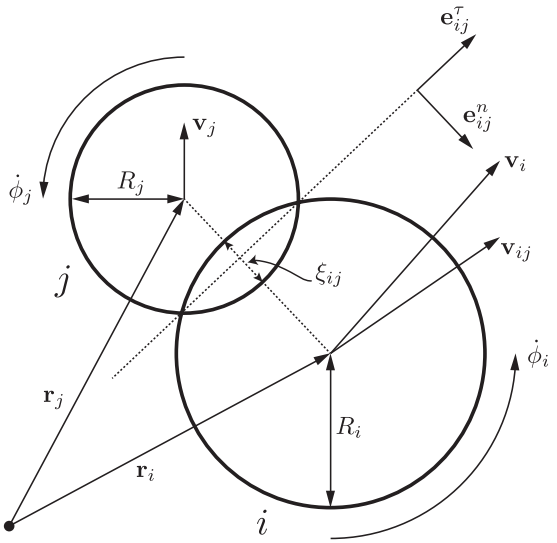

Fig. 1. Sketch indicating the various F–D components for a binary collision between particle i and j.

Table 1
Normal Force–Displacement F^n models based on the extended non-linear viscoelastic model. F^n stands for F_{ij}^n, and ξ stands for ξ_{ij}.

Model no.	Model name	Expression	Ref.
M_1	Tsuji	$F^n = -k^n\xi^{3/2} - \gamma^n\dot{\xi}\xi^{1/4}$	[36]
M_2	Kuwabara–Kono	$F^n = -k^n\xi^{3/2} - \gamma^n\dot{\xi}\xi^{1/2}$	[37,38]
M_3	Extended non-linear	$F^n = -k^n\xi^{3/2} - \gamma^n\dot{\xi}\xi^{\alpha^n}$	[19]

where each particle i, $i = 1, \ldots, N$ has a mass (m_i) and moment of inertia (I_i), translational ($\ddot{\mathbf{r}}_i$) and rotational ($\ddot{\phi}_i$) acceleration while $\mathbf{g}$ denotes gravity, $\mathbf{l}_{ij}$ denotes the vector from the center of particle i to the contact point with particle j and $\mathbf{e}_{ij}^z$ denotes the unit vector perpendicular to the plane spanned by $\mathbf{e}_{ij}^t$ and $\mathbf{e}_{ij}^n$. These ordinary differential equations (Eq. (2)) are solved with a 3rd order Gear Predictor–Corrector scheme [32]. The time-step $\Delta t = 10^{-6}$, allows for the collisions between two disks to be simulated using at least 87 time steps [33]. Note that Timoshenko et al. [34] give an expression for the duration of a collision: $\delta t = 2.9432\frac{C^2 R_{eff}}{u_n}$ where $C = \left(\frac{15 m_{eff} u_n^2}{R_{eff}^3 E_{eff}}\right)$, $R_{eff} = R_i R_j / \left(R_i + R_j\right)$, the effective Young's modulus given as $1/E_{eff} = \left(\left(1-\nu_i^2\right)/E_i + \left(1-\nu_j^2\right)/E_j\right)$, $m_{eff} = m_i m_j/(m_i + m_j)$ and u_n denotes the relative normal velocity between the two particles just before the contact. Following the recommendation in [35], we use a time-step equal to $1/50$ fraction of the shortest possible collision time in the system estimated with the formula for δt above.

In the present work deformations induced by contacts between particles or a particle colliding with a boundary, are modeled by the formation of an overlap region at the contact point while the circular shape is maintained after collisions. Here we employ three F–D models specified by three different normal forces and one single tangential force. These models are based on the F–D model proposed by Tsuji et al. [36] and their functional form and parameters are given in Table 1. The parameters in Table 1 consist of the material property spring constant k^n, given according to Hertz theory as $k^n = 4/3 E_{eff}\sqrt{R_{eff}}$. The dissipative constant γ^n is phenomenological while in the models M_1, M_2 the exponent in the dissipative terms is a-priori specified to be $1/4$ and $1/2$ respectively. In the third model M_3, the exponent is left to be freely determined as a parameter based on the experimental observations.

The tangential force component is obtained by a modification of the original Cundall and Strack model [39]:

$$F^t = -\left|k^t \xi^t\right| \cdot \operatorname{sign}\left(\xi^t\right), \quad \xi^t = \int_{\tau_0}^{\tau} u_t H\left(\mu \left|F^n\right| / k^t - \left|\xi^t\right|\right) d\tau' \tag{3}$$

where H is the Heaviside function, k^t and μ are phenomenological parameters modeling the tangential spring stiffness and friction, τ_0 is the time when the collision between disk i and j starts, $\tau \geqslant \tau_0$ is the time when we evaluate the force and u_t denotes the relative tangential velocity between the two particles at their contact point. Collisions of particles with rigid walls are represented by collisions with phantom disks with a very small curvature [40]. This method treats the walls as a smooth boundary surface allowing for inelastic collisions.

3. Bayesian uncertainty quantification and propagation for the DEM

We consider a parametrized class M of a Force–Displacement model, and let $\theta \in \mathbf{R}^{N_\theta}$ be a set of F–D parameters (e.g. tangential spring stiffness, friction coefficient, dissipative constant) belonging to this model class, that will be estimated using experimental data. The model parameters θ are considered to be uncertain and probability distribution functions (PDF) are introduced to quantify their plausible values. A PDF $\pi(\theta|M)$ is assigned to the model parameters incorporating prior information based on previous knowledge or physical limitations.

3.1. Model parameter estimation

In Bayesian inference, the probability distribution of the model parameters θ is updated based on measurements available at a particle–particle, particle–wall or system level. Let $D \equiv \hat{y} = \{y_r, r = 1, \ldots, n_y\} \in \mathbf{R}^{n_y}$ be a set of observations (data) available from experiments. The prediction error $e \in \mathbf{R}^{n_{\hat{y}}}$ is introduced to characterize the discrepancy between the model predictions $g(\theta|M) \in \mathbf{R}^{n_y}$ and the corresponding data $\hat{y}$. The observation data and the model predictions satisfy the prediction error equation

$$\hat{y} = g(\theta|M) + e. \tag{4}$$

The prediction error is composed of two parts

$$e = e^d + e^m, \tag{5}$$

accounting for the measurement (e^d) and modeling (e^m) uncertainties, respectively.

Experimental data usually are provided in terms of the mean and the variance of each measured quantity so the maximum entropy principle [41], can be invoked to select a normal distribution for the measurement error term e^d. Similarly, this Gaussian assumption is also well justified for the modeling error term e^m due to the lack of information for assigning an alternative distribution.

Assuming zero mean for each error term, we set $e^d \sim N\left(0, \Sigma^d\right)$ and $e^m \sim N(0, \Sigma^m)$, where Σ^d, and Σ^m are taken to be diagonal, due to the fact that measurements and model predictions under different system conditions are independent. The covariance matrix $\Sigma^d = diag\left(\tilde{v}_r^2\right)$, where $\tilde{v}_r^2$ is the variance of the rth observation. The covariance matrix $\Sigma^m = diag\left(\sigma_r^2 \hat{y}_r^2\right)$ of the model error term involves the unknown normalized variance parameters σ_r^2 which are usually included in the uncertain parameter set θ to be determined from the data. It represents the inability of the model to capture all of the experimental values at all possible scenarios. Letting $\sigma_r^2 = \sigma^2$ one obtains the covariance matrix $\Sigma^m = \sigma^2 diag(\hat{y}_r^2)$ involving a single parameter σ^2, scaling the variances of each prediction error quantity involved in e^m by its experimental value $\hat{y}_r^2$. Note that Bayesian results depend on the choices of the distributions and the correlation structure of the modeling errors. However a detailed study of different assumptions on the distribution of the modeling terms is beyond the scope of the current study. The reader is referred to Ref. [42] for the effect of correlation structure of the covariance matrix on the Bayesian results.

The updated distribution $f(\theta|D, M)$ of the model parameters θ, given the data D, the model class M and prior information about the parameters $\pi(\theta|M)$, is given from the Bayes theorem as

$$f(\theta|D, M) = \frac{f(D|\theta, M)\, \pi(\theta|M)}{f(D|M)} \tag{6}$$

where $f(D|\theta, M)$ is the *likelihood* of observing the data D from a model corresponding to a value θ of the model class M and $f(D|M)$ is the *evidence* of the model class M, selected such that the posterior distribution $f(\theta|D, M)$ of the model parameters integrates to one.

Using the prediction error equation (4) and assuming that the error terms in (5) are independent, the likelihood $f\,(D|\theta, M)$ of observing the data follows the multi-variable normal distribution:

$$f\,(D|\theta, M) = \frac{\left|\Sigma^{-1/2}\right|}{(2\pi)^{N/2}} exp\left[-\frac{1}{2} J\left(\theta; \hat{y}\right)\right] \tag{7}$$

where

$$J\left(\theta; \hat{y}\right) = \left[\hat{y} - g\,(\theta|M)\right]^T \Sigma^{-1} \left[\hat{y} - g\,(\theta|M)\right] \tag{8}$$

is the weighted measure of fit between the F–D model predictions and the measured data, $\Sigma = \Sigma^d + \Sigma^m = diag[\tilde{v}_r^2 + \sigma_r^2 \hat{y}_r^2]$ is the covariance of the prediction error, and $|.|$ denotes a determinant.

Stochastic simulation algorithms are used to generate samples from the posterior PDF. Here we use the TMCMC algorithm [28], a generalization of the methods proposed in [23,43]. To handle the large computational cost associated with the TMCMC algorithm, we exploit the parallel nature of the algorithm [29] using a task-stealing library [30].

3.2. Force–displacement model selection

Following the Bayesian calibration of the F–D model, selection between two alternative model classes M_i and M_j, based on the observed data D, can be guided using the Bayes factor [22]

$$K_{ij} = \frac{f(D|M_i)}{f(D|M_j)}. \tag{9}$$

A number of μ competing model classes $M_1, \ldots, M_\mu$ are ranked based on their probability given the data D according to the Bayes model selection equation

$$Pr(M_i|D) = \frac{f(D|M_i)\,Pr(M_i)}{f(D|M_1, \ldots, M_\mu)} \tag{10}$$

where $Pr(M_i)$ is the prior probability of the model class M_i. The most probable model class is selected as the one that maximizes $Pr(M_i|D)$ over i. The evidence of each model class is evaluated as a by-product of the TMCMC algorithm.

3.3. Uncertainty propagation for robust posterior predictions

Robust posterior predictions of an output QoI Q are obtained by taking into account the updated (posterior) uncertainties in the model parameters given the measured data D [44]. Within this work, the robust posterior predictions are conditioned to the data driven Bayesian identification of the uncertainties in the models and their parameters [25]. Let $F_Q(q|\theta, M)$ be the conditional cumulative distribution of Q given the model parameters θ and the model class M. For Gaussian modeling and measurement errors, the form of the cumulative distribution is simple and does not require expensive system simulations. For systems that include uncertain initial condition input excitation uncertainties or other stochastic descriptors of its components, the estimation of the conditional cumulative distribution may be computationally very expensive.

The posterior robust cumulative distribution $F_Q(q|D, M)$ of the output quantity Q, taking into account the model M and the data D, is given by

$$F_Q(q|D, M) = Pr(Q \geq q|D, M) = \int_\theta F_Q(q|\theta, M) f(\theta|D, M) d\theta. \tag{11}$$

The robust estimate $F_Q(q|D, M)$ represents an average of the conditional cumulative distribution weighted by the posterior probability distribution $f(\theta|D, M)$ of the model parameters [45]. The posterior cumulative distribution $F_Q(q|D, M)$ quantifies the uncertainty in the QoI Q given the model and the data. Using the samples $\theta^{(i)}$, $i = 1, \ldots, N$ drawn from the posterior probability distribution $f(\theta|D, M)$, the integral (11) is approximated by the sample estimate

$$F_Q(q|D, M) \approx \frac{1}{N} \sum_{i=1}^{N} F_Q(q|\theta^{(i)}, M). \tag{12}$$

Table 2
Dataset for the DEM calibration, containing experimentally measured coefficient of restitution $\hat{y}_r$, both normal (*cnr*) and tangential (*ctr*). The fourth column $\hat{v}_r$ refers to the reported measurement uncertainties for each case. All values are taken from Ref. [46].

Impact angle (deg)	Type	$\hat{y}_r$	$\tilde{v}_r$ (deg)
10	*ctr*	0.523	0.010
20	*ctr*	0.524	0.014
30	*ctr*	0.637	0.044
40	*ctr*	0.779	0.013
50	*ctr*	0.846	0.042
60	*ctr*	0.886	0.024
10	*cnr*	0.890	0.020
20	*cnr*	0.892	0.015
30	*cnr*	0.918	0.014
40	*cnr*	0.896	0.005
50	*cnr*	0.918	0.013
60	*cnr*	0.874	0.033

Eq. (11) and the corresponding sample estimate (12) can be used to provide a robust posterior estimate $Pr(Q \geq q_{level}|D, M) = F_Q(q_{level}|D, M)$ of the probability of the QoI Q exceeding a level q_{level}, taking into account the posterior uncertainties in the model parameters given the data D and the model class M, as well as the model prediction errors.

Let $G(Q)$ be a function of the output QoI Q. The posterior robust performance measure of $G(Q)$ given the data D is estimated from [44]:

$$E\left[G(Q)|D, M\right] = \int E\left[G(Q)|\theta, M\right] f(\theta|D, M) d\theta. \tag{13}$$

Setting $G(Q) = Q$ or $G(Q) = (Q - E[Q|D, M])^2$ in (13) and approximating the integral by its sample estimate we obtain [29] the posterior robust mean

$$\bar{\mu}_Q \equiv E\left[Q|D, M\right] \approx \frac{1}{N} \sum_{i=1}^{N} \mu_Q\left(\theta^{(i)}; M\right) \tag{14}$$

and the posterior robust variance

$$\begin{aligned} \bar{\sigma}_Q^2 &= E\left[\left(Q - \bar{\mu}_Q\right)^2 |D, M\right] \\ &\approx \frac{1}{N} \sum_{i=1}^{N} \sigma_Q^2(\theta^{(i)}; M) + \frac{1}{N} \sum_{i=1}^{N} \left[\mu_Q(\theta^{(i)}; M) - \bar{\mu}_Q\right]^2 \end{aligned} \tag{15}$$

of the output QoI Q. The posterior PDF in (12), the posterior mean in (14) and the posterior variance in (15) constitute robust measures of uncertainty of the QoI Q given the models and the data, taking into account the modeling and parametric uncertainties. The coefficient of variation COV(Q), defined as the ratio of the standard deviation $\bar{\sigma}_Q$ to the mean values $\bar{\mu}_Q$ constitutes also an alternative measure of the uncertainty in the QoI Q.

4. Bayesian uncertainty quantification for contact-force models

We perform DEM simulations of a disk colliding with a steel wall and employ the Bayesian framework to quantify uncertainties in the parameters of the three F–D models. Furthermore we provide a method to select the most probable F–D model as well as propagate uncertainties to predict various output QoIs.

The Bayesian framework quantifies uncertainties in these parameters based on the experimental values and their uncertainties for disk particles of steel colliding in a same material steel wall (see Table 2). The steel material and geometric properties of the particles used in this study are: Young modulus $E = 2.10 \cdot 10^{10}$, Poisson ratio $\nu = 0.3$,

Table 3
Range of uniform prior PDFs $\pi(\theta)$ of the model parameters for all three model classes.

Class	Support of prior PDF $\pi\ (\theta)$
M_1	$[0.05, 0.2] \times [0.1, 15.0] \times [0.1 \cdot 10^4, 15.0 \cdot 10^4] \times [0, 1 \cdot 10^{-2}] \times [0, 1 \cdot 10^{-2}]$
M_2	$[0.05, 0.2] \times [0.1, 15.0] \times [0.1 \cdot 10^4, 15.0 \cdot 10^4] \times [0, 1 \cdot 10^{-2}] \times [0, 1 \cdot 10^{-2}]$
M_3	$[0.05, 0.2] \times [0.15, 1.35] \times [0.1, 15.0] \times [0.1 \cdot 10^4, 15.0 \cdot 10^4] \times [0, 1 \cdot 10^{-2}] \times [0, 1 \cdot 10^{-2}]$

Table 4
Mean values and coefficients of variation (COV) of the posterior distribution of the model parameter, along with the LogEvidence values of each model class.

Class	$\bar{\mu}$	u_μ	$\bar{\alpha}^n$	u_{α^n}	$\bar{\gamma}^n$	u_{γ^n}	$\bar{k}^t$	u_{k^t}	σ_1	σ_2	LogEvidence
M_1	0.109	12.8%	0.25	–	$0.81 \cdot 10^4$	17.2%	0.99	35.1%	0.0045	0.0016	15.46
M_2	0.108	11.77%	0.5	–	$8.41 \cdot 10^4$	18.7%	1.01	33.8%	0.0035	0.0019	16.39
M_3	0.111	9.5%	0.44	5.78%	$5.45 \cdot 10^4$	55.5%	1.04	27.9%	0.0045	0.0007	22.41

disk radius $R_i = 0.02225$ m with a mass of 0.3538 kg. Note that these are the values reported in the experimental study, but are not necessarily exact. One could consider them uncertain, and identify them along with the other model parameters.

The mean values and the experimental uncertainty in the restitution coefficient measurements are reported in Table 2 for various values of the impact angle between steel particles and a steel wall. We use as data the coefficients of tangential (*ctr*) and normal (*cnr*) restitution for six values of the impact angle ranging from 10 to 60 degrees. The coefficient of normal restitution is the ratio of the post-collisional and the pre-collisional values of the normal component of the relative velocity of the object [47]. Similarly the coefficient of tangential restitution is the ratio of the tangential velocity components.

The covariance $\Sigma^m = diag\left(\Sigma^m_{cnr}, \Sigma^m_{ctr}\right)$ of the prediction error model is chosen as a 2×2 block diagonal matrix with each block associated with the *ctr* and *cnr* measurements. The diagonal block elements Σ^m_{cnr} and Σ^m_{ctr} are also assumed to be diagonal matrices, i.e. $\Sigma^m_{cnr} = \sigma_1^2 diag\left(\hat{y}^2_{cnr}\right)$ and $\Sigma^m_{ctr} = \sigma_2^2 diag\left(\hat{y}^2_{ctr}\right)$, dividing in this way the data into two disjoint groups associated with the normal and tangential coefficient of restitution, respectively. Each group of data involves six measurements and the prediction errors for each one of the measurements are assumed to be independent. Note that the parameter k^n was kept fixed to its theoretical value determined using the Young modulus, the Poisson ratio and the radius of the considered disks. Although one could have included the parameter k^n in the uncertain vector θ, herein it was decided to keep it fixed to its theoretical value, thus avoiding possible strong interactions between this parameter and the rest of the F–D model parameters that could result in unrealistic k^n values further away from the theoretical one.

For the model classes M_1 and M_2 the parameter vector is $\theta = \left(\mu, \gamma^n, k^t, \sigma_1, \sigma_2, \right)$ involving 3 F–D model parameters, and two prediction error parameters. The θ for the third model class is $\theta = \left(\mu, \alpha^n, \gamma^n, k^t, \sigma_1, \sigma_2, \right)$, including the exponent α^n as an extra parameter. Uniform prior distributions for all parameters are used and their ranges are shown in Table 3.

A parallel TMCMC algorithm [29] is used to generate samples from the posterior PDF of the model parameters. A sensitivity study for the selection of the number of samples per TMCMC stage was performed, indicating that 8192 samples were adequate for all model classes considered, since an increase of almost 2 order of magnitude in samples yielded results that differ insignificantly. The posterior distribution of the model parameters were thus represented by the 8192 samples obtained at the last TMCMC stage.

The marginal distributions of the parameters for the three model classes M_1, M_2 and M_3 (see Figs. 2–4) are obtained using Kernel estimation. The TMCMC samples drawn from the posterior distribution provide sample estimates of the mean and the standard deviation of the model parameters using Eqs. (14) and (15), respectively. The posterior mean $\bar{\theta}$ and the coefficient of variation (COV) u_θ of the model parameters are reported in Table 4 for each model class. The COV measures the extent of uncertainty which is defined as the ratio of the sample standard deviation over the sample mean.

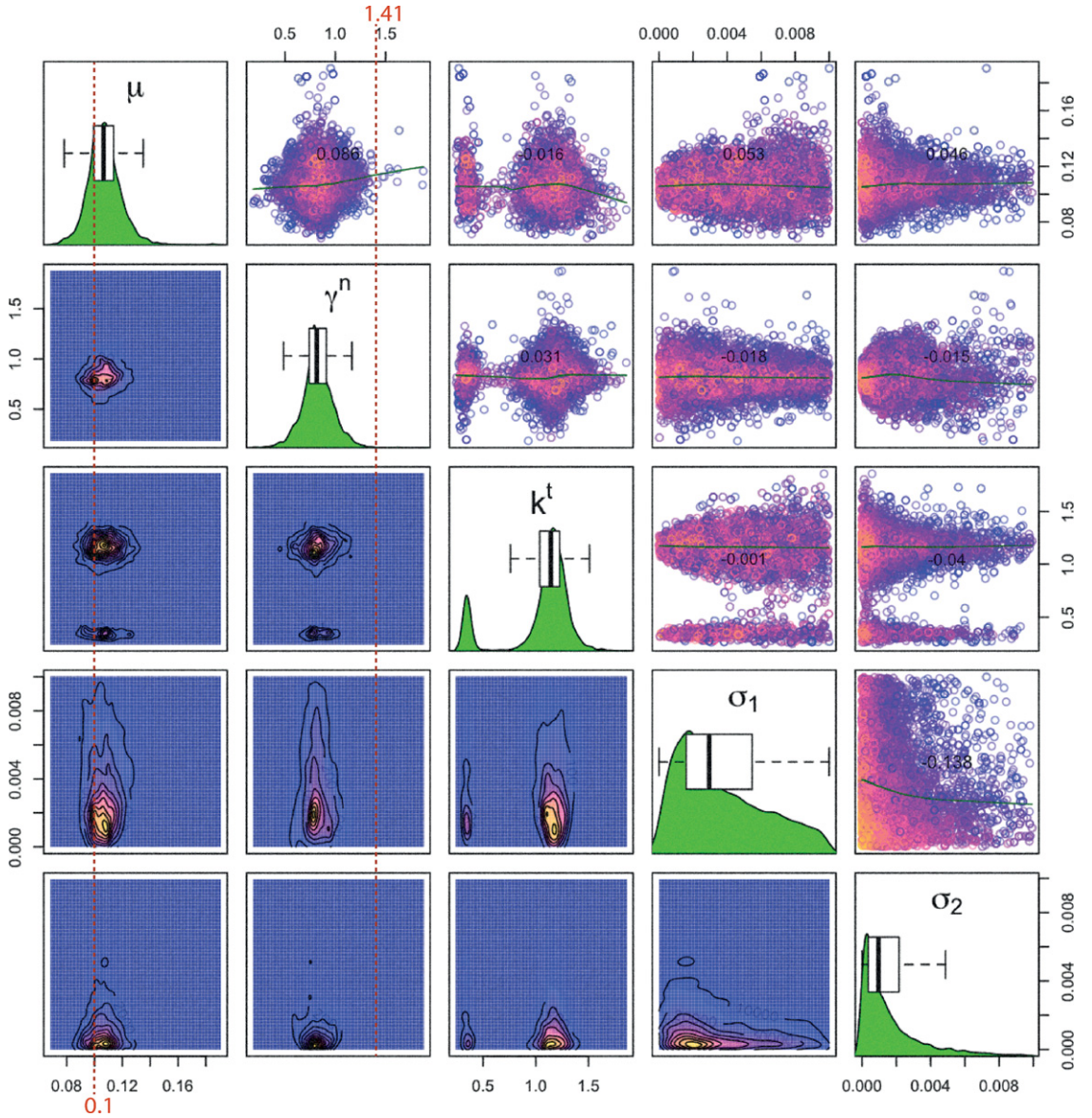

Fig. 2. Bayesian Calibration results for M_1. Above the diagonal: Projection of the TMCMC samples of the posterior distributions $f(\theta|D, M_1)$ in all pairs of 2-d parameter space (Colors indicate LogLikelihood values of the samples). Diagonal: Marginal distributions of the model parameters estimated using kernel histograms. Box-plots demarcate the mean and 95% percentiles. Below the diagonal: Projected densities in 2-d parameter space constructed via a bicubic kernel estimate (Coloring according to PDF Log-values). (For interpretation of the references to color in this figure legend, the reader is referred to the web version of this article.)

The TMCMC samples from the last stage of the algorithm drawn from the posterior distribution employing the force–displacement model class M_1 are presented in Fig. 2. The posterior marginal distributions of the model parameters γ^n and μ appear to be approximately symmetric with a sizeable uncertainty of COVs of 17.2% and 12.8% respectively as indicate in Table 4. The marginal distributions of the prediction error parameters σ_1 and σ_2 are asymmetric with positive tail distributions. From the results in Table 4, the mean values of the prediction errors are 6.7% and 4.0% for σ_1 and σ_2, respectively.

Strikingly different is the behavior of the F–D parameter k^t. Inspection of the marginal PDF of k^t reveals a clearly bimodal nature, with two distinct peaks, around $k^t \approx 0.4$ and $k^t \approx 1.33$. The peak value at $k^t \approx 1.33$ is approximately 2.1 times more probable than the peak value at $k^t \approx 0.4$. In order to understand this bimodal nature, we calculate the

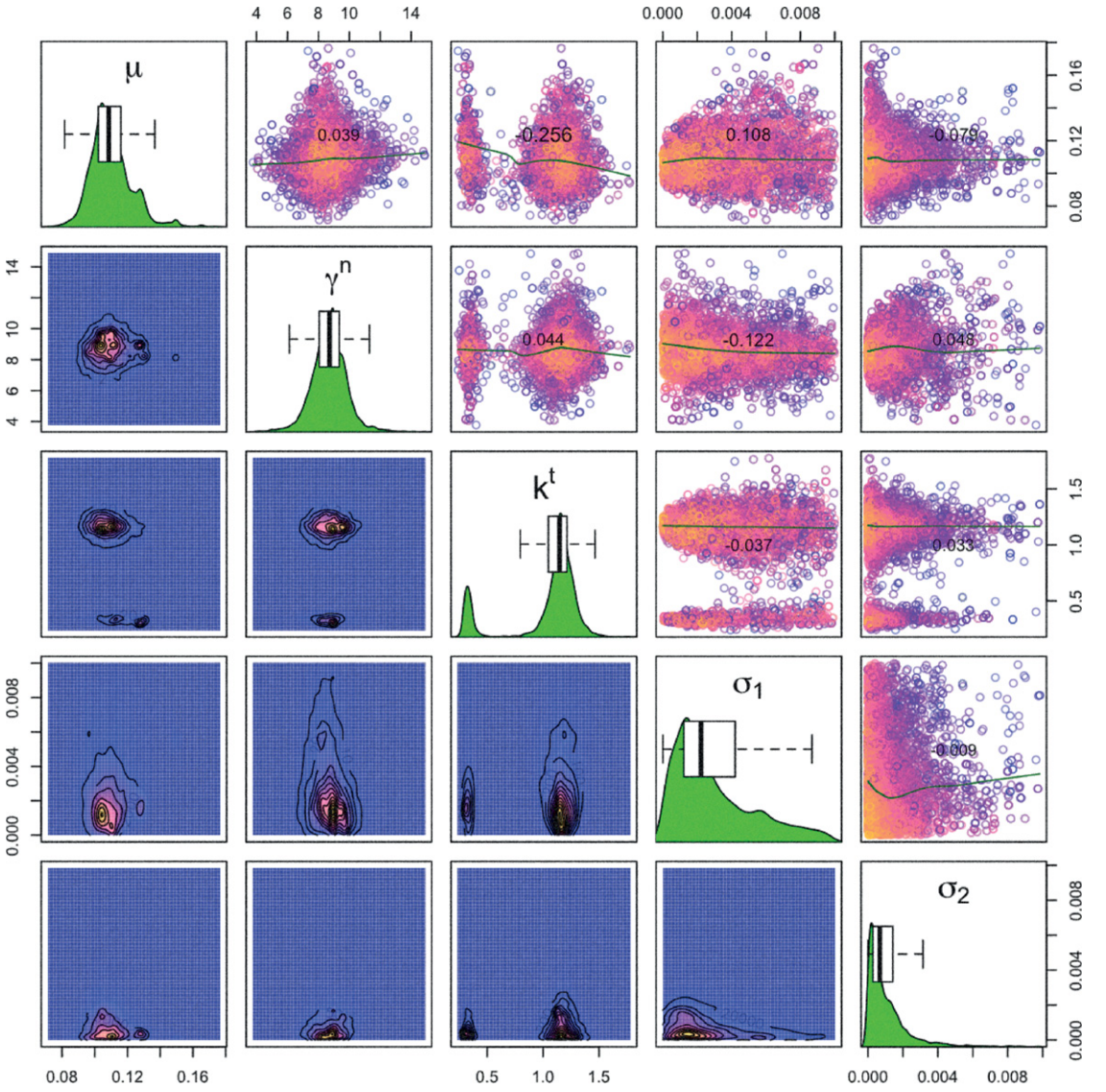

Fig. 3. Bayesian Calibration results for M_2. Color scheme and plot layout as in Fig. 2. (For interpretation of the references to color in this figure legend, the reader is referred to the web version of this article.)

robust predictions of the *ctr*, from each one of the two well-separated modes of the marginal distribution of k^t shown in Fig. 5.

The robust predictions of *ctr* using the samples around the mode peaked at $k^t \approx 0.4$ are shown in Fig. 5(a), while the robust prediction of *ctr* using the samples around the mode peaked at $k^t \approx 1.33$ are shown in Fig. 5(c). The samples from the two modes make almost the same quantitative predictions of the uncertainty in the *ctr* values for the four higher impact angles. However, the predictions of the uncertainties for lowest two *ctr* values and the variation of the *ctr* values and their uncertainties as a function of impact angles for impact angles lower than 20 degrees are qualitatively different. This bimodality is clearly a result of an inadequate number of experimental data available at the lower impact angle values. This finding suggests that experimental results for impact values lower than 10 degrees would lead to a more informed (and unimodal) posterior distribution.

The uncertainty in the parameter estimates of the model class M_2 are shown in Fig. 3. The two model classes M_1 and M_2 differ solely on the exponent in the displacement damping term. Comparing Figs. 2 and 3 and the values reported in Table 4, it can be seen that the calibration results between M_1 and M_2 are quantitatively very similar for the

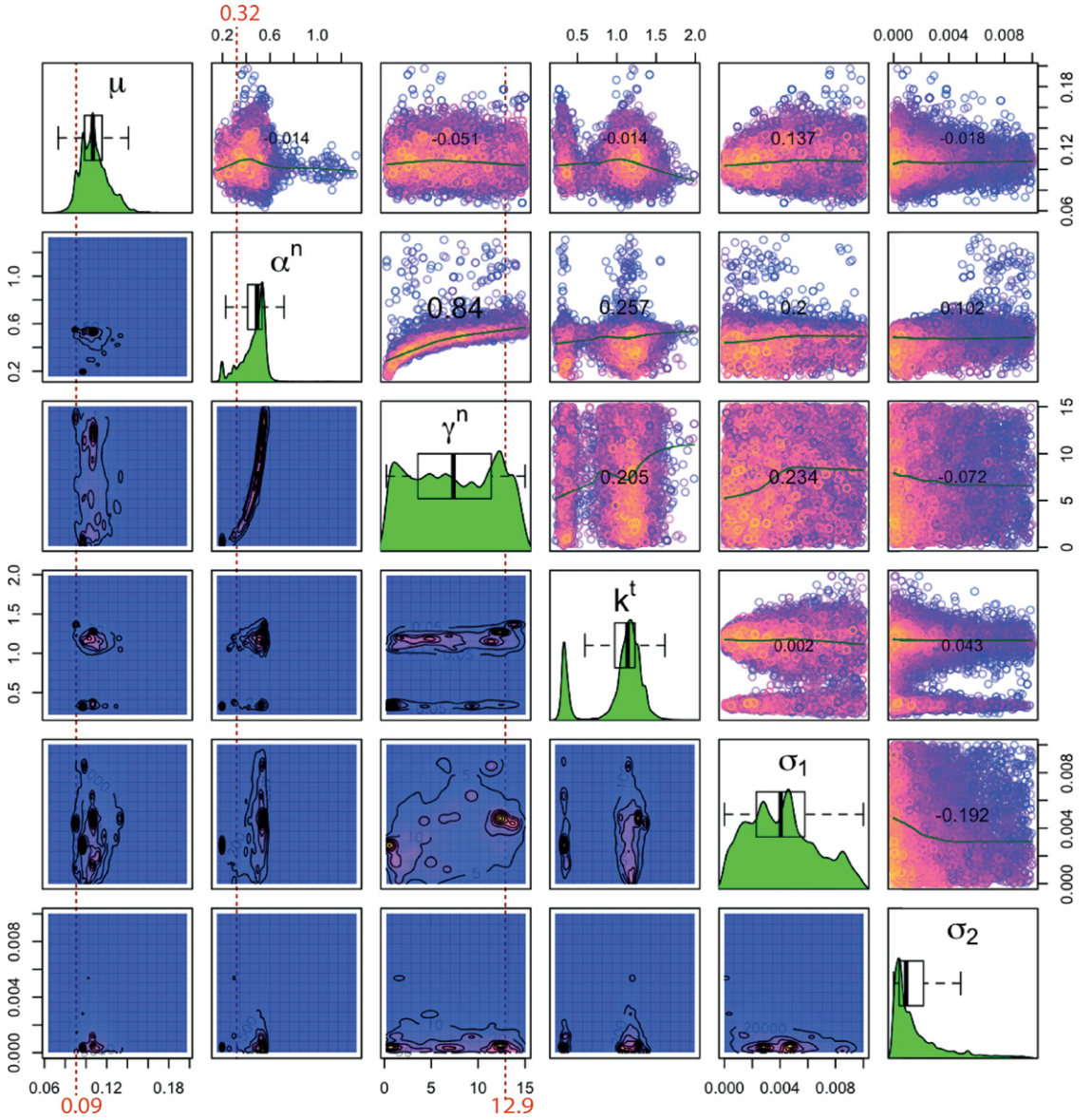

Fig. 4. Bayesian calibration results for M_3. Color scheme and plot layout as Fig. 2. (For interpretation of the references to color in this figure legend, the reader is referred to the web version of this article.)

two out of the three F–D model parameters μ and k^t. The prediction error parameters σ_1 and σ_2 are also quantitatively similar for the two model classes. The mean values in Table 4 suggest that σ_1 is 10% higher and σ_2 is 10% lower for the model class M_1 than the corresponding values for the model class M_2. Significant differences are estimated only for the parameter γ^n, which has a MAP estimate of 8.41 for model class M_2 compared to 0.81 for the model class M_1. This is due to the different displacement exponent damping term in the F–D model used for the model classes M_1 and M_2. This indicates that the value of the exponent significantly affects the magnitude of the damping term. In the model class M_3 the exponent is left free to be determined from the data.

The shape of the marginal distributions and the projections in the 2-d spaces shown in Figs. 2 and 3 indicate that, with the exemption of the γ^n parameter, the model class M_2 has identical behavior to M_1, including the bimodality in κ_t. The similarities between F–D models M_1 and M_2 can also be corroborated from their Model Evidence values reported in Table 4. Using the Bayes factor (9) and assuming equal priors for the two model classes, the relative probabilities of the model classes M_1 and M_2 are 0.28 and 0.72, respectively. These probabilities slightly promote M_2

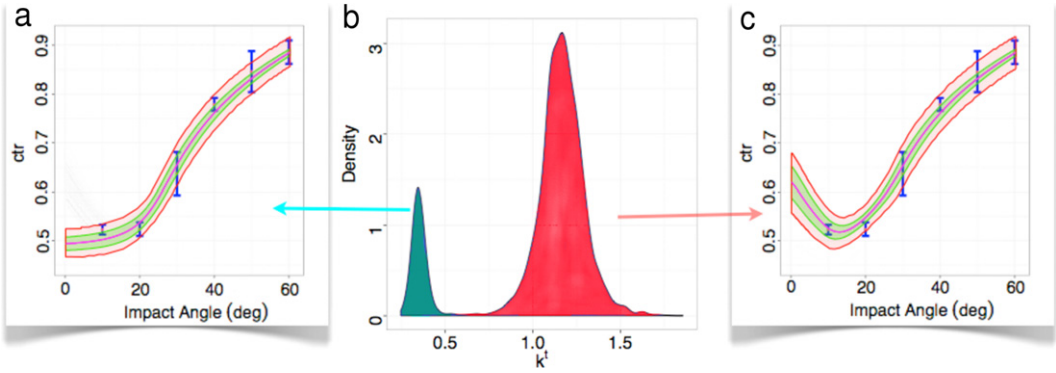

Fig. 5. Uncertainty Propagation for *ctr* using model class M_1. (a) Propagation using samples around the mode peaked at $k^t \approx 0.4$. (b) Bi-modal marginal distribution of k^t. (c) Propagation using samples around the mode peaked at $k^t \approx 1.33$.

as more probable than M_1, but are not sufficiently different so as to disregard the importance of model class M_1 in Bayesian predictions.

The calibration results for model class M_3 are presented in Fig. 4. From the 2-D projection in the parameter space (γ^n, α^n), the parameters γ^n and α^n appear highly correlated. The uncertainty region is confined within a two-dimensional manifold in the 6-D parameter space. From this 2-D projection in (γ^n, α^n) space it is apparent that the parameter γ^n is unidentifiable with most probable values ranging over the whole domain of variation from 0.1 to 15 considered in the prior distribution. The optimal values and the uncertainty regions for the γ^n parameter predicted by model classes M_1 and M_2 are clearly subsets of the values predicted by the model class M_3 and contained within the unidentifiable manifold. It is worth pointing out that the optimal values along the unidentifiable manifold give same predictions of the measured quantities. The optimal parameter values and associated uncertainties estimated for the F–D model parameters μ and k^t (Table 4) are quantitatively very similar to the values obtained for the first two model classes M_1 and M_2. Moreover, the bimodality in k^t observed for model classes M_1 and M_2 is preserved for the model class M_3 as well. The prediction error parameters σ_1 and σ_2 are quantitatively similar for the three model classes. Finally, comparing the model evidence values for M_1, M_2 and M_3, it is apparent that M_3 is promoted as the single most probable model class with relative posterior probability equal to unity. Clearly there is flexibility in the selection of the values of the F–D exponent α^n used for model classes M_1 and M_2 (Table 2). Any value between 0.15 and 0.6 could have been used, provided that the value of γ^n is adapted accordingly using the information from the manifold of these two unidentifiable parameters.

5. Uncertainty propagation

Following the Bayesian calibration, the uncertainties identified for the parameter vector θ, using experimental values from the collision of a sphere with a wall are propagated in order to make robust predictions of various QoIs extracted from DEM simulations. We consider three problems:

- a steel disk impacting a steel wall, with or without initial spin.
- the Brazil Nut effect
- silo discharge

It is assumed that all particles involved share identical material properties.

5.1. Disk impacting a wall: robust prediction of restitution coefficient

Using the prediction error model employed and Eq. (15) we predict the normal and tangential coefficients of restitution of a steel disk impacting a steel wall using the 8192 posterior samples. The mean values and standard deviation of the posterior distribution of coefficients of tangential restitution are shown in the top three subplots of Fig. 6 as a function of the impact angle for the three model classes M_1, M_2 and M_3. Similar results for the coefficient of normal restitution as a function of the initial impact velocity normal to the wall are shown in the bottom three subplots

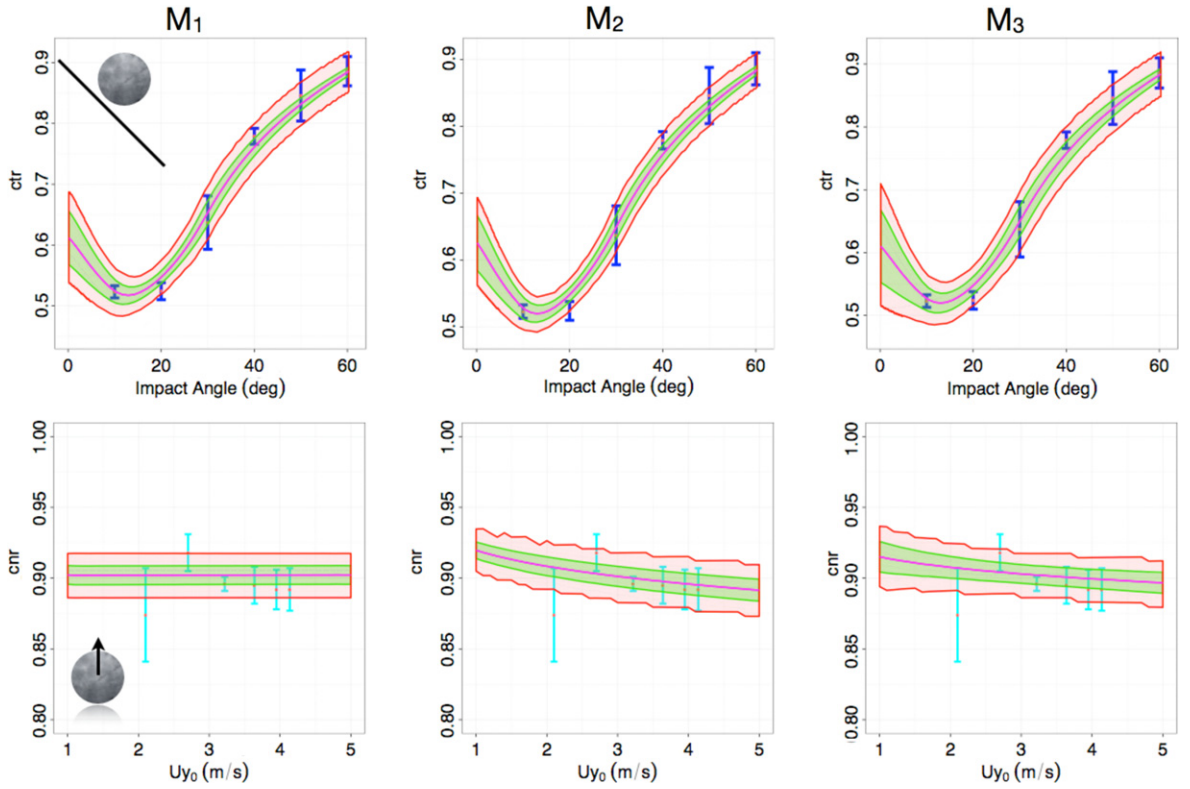

Fig. 6. Uncertainty Propagation for *ctr* and *cnr* using model classes M_1, M_2 and M_3. Propagation to the calibrated values, top—*ctr*, bottom—*cnr*. Experimental Values and their uncertainties are depicted in blue. Magenta lines indicate the mean prediction, green shaded areas show the parameter uncertainty contribution, and red is the total uncertainty using the prediction error model employed and Eq. (15). (For interpretation of the references to color in this figure legend, the reader is referred to the web version of this article.)

of Fig. 6. We find that the model error uncertainty is of equal importance as the parametric uncertainty. The predictions containing parametric uncertainties underestimate the uncertainties in the experimental values. The experimental uncertainties considered in the calibration process are well captured, as should be expected, by considering both the parametric and model error uncertainties.

Uncertainty propagation results for the coefficient of tangential restitution are presented for the case where an initial spin of 80 rad/sec is given to the steel particle. The *ctr* uncertainties predicted by the model are shown as a function of the impact angle in Fig. 7 for all model classes and for two types of uncertainty cases. In the first case, only parametric uncertainties identified by the calibration procedure based on the *ctr* and *cnr* experimental values without spin are propagated. In the second case, both parametric and model error uncertainties are propagated. In the latter case, the model errors are assumed to be independent, identically distributed zero-mean Gaussian variables with standard deviation equal to 8% of the estimated mean values. The model prediction uncertainties are compared with the uncertainties in the experimental values of the restitution coefficients for various impact angle values available in the literature for particles with the same spin [46]. The variation of the model predicted mean values of *ctr* as a function of the impact angle adequately represent the observed variation in the experimental values. However, the uncertainty in the *ctr* due to the uncertainties in the parameters of the F–D model is relatively small and cannot adequately capture the observed uncertainty in the experimental values. The uncertainty in the experimental values can be captured by introducing an 8% model error uncertainty.

These results emphasize the importance of including model error uncertainties in making robust predictions of output QoI in DEM simulations. Propagation of the identified uncertainty in the model parameters alone for predicting various unobserved QoI is not adequate to make informed robust predictions. Model error uncertainty, resulting from the inadequacy of the mathematical model class to represent an output QoI, need also to be quantified and considered in the predictions. Introducing adequate mathematical models for quantifying model errors is quite challenging since

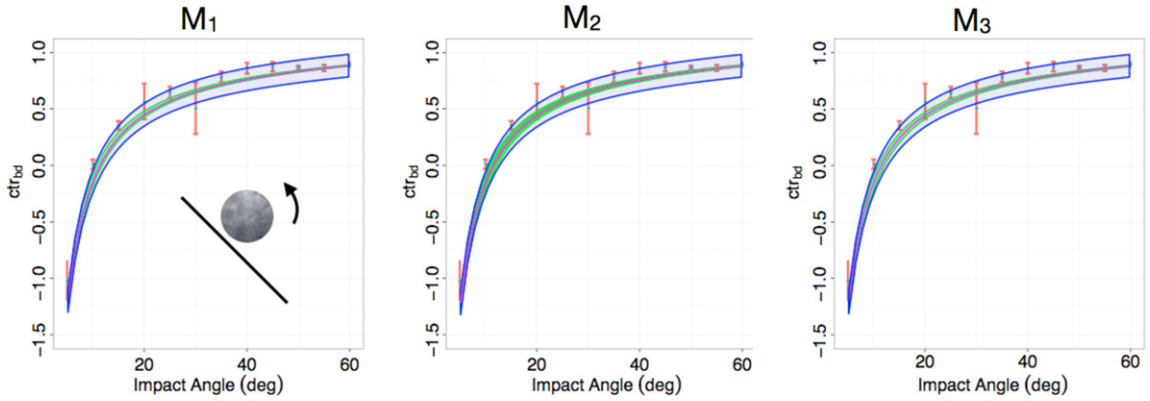

Fig. 7. Uncertainty Propagation for *ctr* using model classes M_1, M_2 and M_3. Prediction based on the plausible values for the backdrop experiment using M_1, M_2 and M_3. Experimental measurements and their uncertainty are depicted in red. Magenta lines indicate the mean prediction, green shaded areas show the uncertainty due to parameters uncertainty, and blue is the total uncertainty using the prediction error model employed and Eq. (15). (For interpretation of the references to color in this figure legend, the reader is referred to the web version of this article.)

observation for all QoI are not available to justify the model error selection. The choice of the mathematical form of these model errors and the values of the parameters involved should be based on experience. In this study, it was reasonable to choose a Gaussian model to represent the expected model error for *ctr* values of impacting particles with initial spin. The level of uncertainty (standard deviation of the Gaussian model error) was another free parameter to be selected. In the absence of experimental data this choice is arbitrary. However, one can investigate the effect of the level of the model error uncertainty on the prediction of the total uncertainty in the QoI. These observations are applicable to all F–D model classes employed herein.

5.2. Brazil nut

We consider a system of 72 identical steel disks of diameter 0.02 m, as well as one disk twice as big representing the "Brazil Nut" (BN). We encage the disks in a rectangular box of width 0.161 m and height 0.32 m, as seen in Fig. 8(a). The box is assumed to be of the same material as the beads. The box is shaken according to the following equations:

$$\vec{x}_c(t) = \begin{bmatrix} r_1 \cos(a_1 t) \\ r_2 \sin(a_1 t) \end{bmatrix}, \qquad \alpha(t) = \frac{2\pi}{180} \sin(a_2 t), \tag{16}$$

where $\vec{x}_c(t)$ is the displacement of the center and α is the orientation angle of the box as seen in Fig. 9(a). The values of the parameters involved in (16) are fixed to $r_1 = 0.05$, $r_2 = 0.083$, $a_1 = 17$ and $a_2 = 180$ for the whole uncertainty propagation procedure.

We define as $p(z, \theta) = t/t_0$ the fraction of time that the nut remains above a certain height z during a shaking that lasts t_0 seconds. The QoI is the height z_p corresponding to a given value for p. Simulations of the system are performed using the model class M_3. Representative sample trajectories starting from two different initial points z_{init}, located at the middle of the box at $z_{init} = 0.02$ and $z_{init} = 0.1$, are shown in Fig. 9(b). Fig. 8 shows 4 different phases of the shaking procedure.

The uncertainty in the height $z_p(\theta)$ as a function of the fraction of time p of exceeding the level $z_p(\theta)$ is given in Figs. 10(a) and (b) for two initial positions of the nut at $z_{init} = 0.02$ and $z_{init} = 0.1$, respectively. The uncertainty is quantified by the mean value of the height $z_p(\theta)$ with respect to θ, as well as the 5% and 95% credible intervals. We have used 500 samples of the posterior distribution in order to propagate parametric uncertainty. The selection of 500 samples is done with weighted Poisson sampling from the 8192 posterior samples with their weight chosen to be their posterior values. The COV $(z_p(\theta))$ of the height z_p due to the parametric uncertainty is also shown in Figs. 10(c) and (d) for $z_{init} = 0.02$ and 0.1, respectively. As expected, the height z_p is a decreasing function of the fraction of time p. From the values of the COV we remark the tendency for the uncertainty in z_p to increase as the fraction of time p is increasing. The COV values for these two particular z_{init} simulation cases range from values as low as 4% for small fractions of time p to values as high as 16% for higher p values. It is clear that the uncertainty in the F–D model parameter values has an effect on this particular QoI.

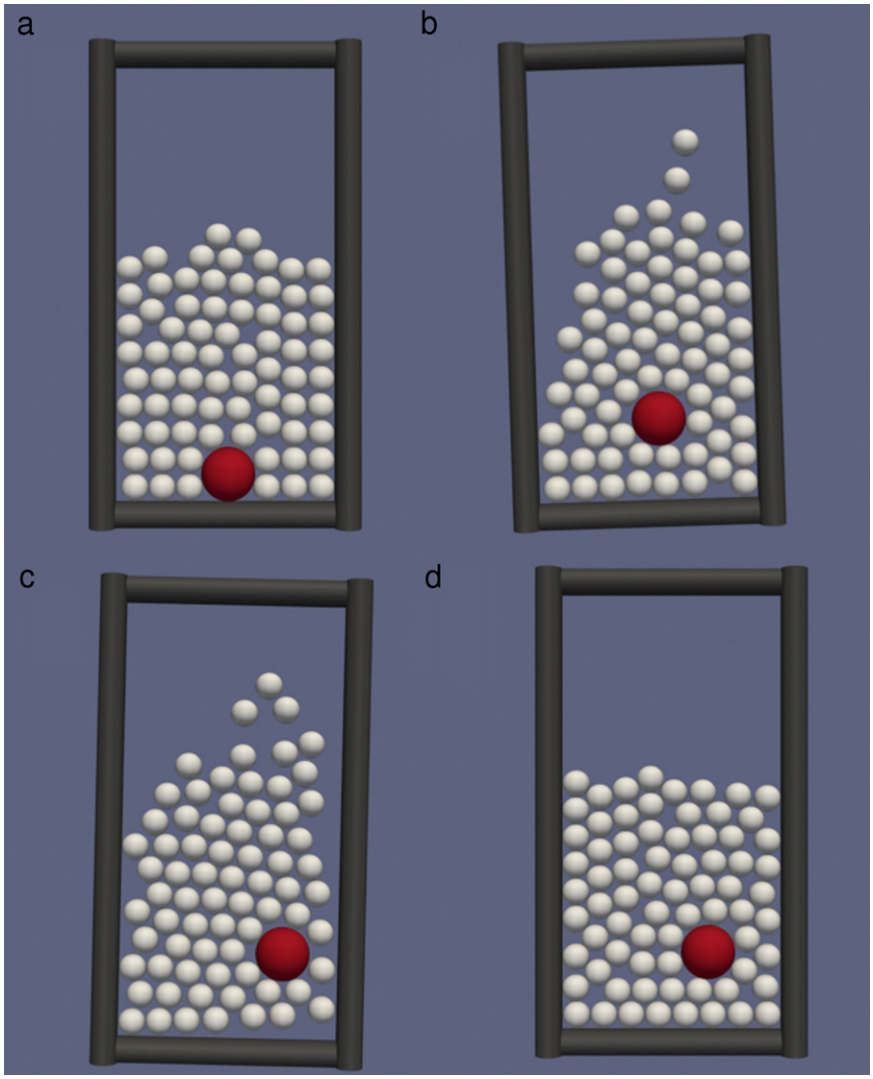

Fig. 8. Shaking pattern: (a) Initial resting position of the Brazil nut at $t = 0$. (b)–(c) Snapshots during the shaking at $t = 10.04$ and 23.04 s. (d) Final resting position of the nut. Smaller steel particles are depicted white, while the "Brazil" nut is red. A video of the shaking can be seen in the Supplementary Video 1 (see Appendix A). (For interpretation of the references to color in this figure legend, the reader is referred to the web version of this article.)

A second QoI is the exit time or the first passage time $t_{exit}(z, \theta)$ of the Brazil nut, defined as the time it takes for the nut to reach a height z for the first time. Fig. 11(a) shows the predictions of the uncertainty in the exit time $Q_t(\theta, z)$ due to the uncertainty in the parameter vector θ as a function of the height z for the case where the initial nut position is $z_{init} = 0.02$. The mean (robust) predictions $t_{exit}(z)$ taking into account the parametric uncertainty as well as those including the overall uncertainty in terms of the 5% and 95% percentile values are shown in this figure. Fig. 11(c) shows the COV$(t_{exit}(\theta, z))$ of the mean exit time due to the parametric uncertainty. Similar results for $z_{init} = 0.1$ are shown in Figs. 11(b) and (d). Note that for the case of $z_{init} = 0.02$, the COV is negligible for height values up to $z = 0.14$, while for height values greater than $z = 0.14$ the COV is approximately 0.3. The negligible uncertainty for low height values is due to the violent motion exerted to the box, causing at the first cycle of vibration the particles and the nut to be lifted inside the box up to a height of 12 cm without interacting with each other. Thus the motion of each particle does not depend on the force–displacement model and the uncertainty in the model parameters do not affect the motion. After the first cycle of box oscillation, the particles and the nut come in contact with each other and the force–displacement model plays a role in the motion of the particle. As it can be seen in Fig. 11(a), the uncertainty in

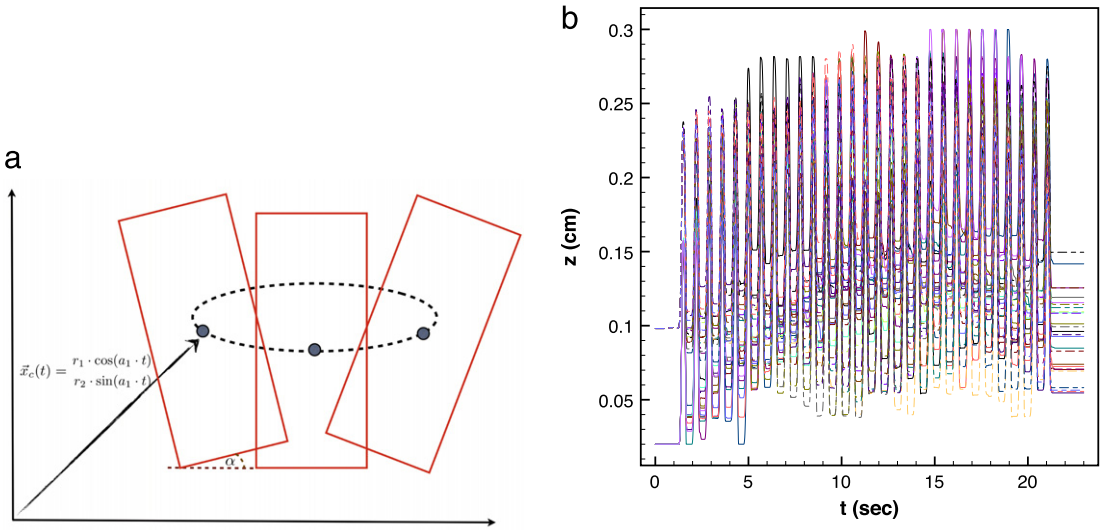

Fig. 9. (a) Box shaking pattern. The center of mass of the box is being moved according to Eqs. (16). (b) Sample trajectories regarding the Brazil nut height during a shaking cycle, from the two starting positions at $z_{init} = 0.02$ (solid lines) and $z_{init} = 0.1$ (dashed lines).

the model parameters plays a significant role in the motion of the particles and the nut, resulting in a large uncertainty with COV $= 0.3$ for the exit time of heights higher than $z = 0.14$. This observation is also confirmed by the results obtained for the simulation case for which the nut initiates from $z_{init} = 0.1$. In the first cycle of box oscillation, the nut is lifted due to the violent motion to a height $z = 0.22$ without interacting with the other particles. Thus the exit time for the first cycle and up to height $z = 0.22$ is not affected by the force–displacement model, yielding negligible uncertainty in the exit time up to the height $z = 0.22$. After the first cycle of box oscillation, the nut and the particles interact and the force–displacement model is activated and governs the motion of the particle. The exit time for heights higher than $z = 0.22$ involves large uncertainty with COV values ranging from 0.2 to 0.8.

The third QoI is the cumulative probability that the exit time exceeds a time instant t. The cumulative probability taking into account the parameter uncertainty is given by Eq. (11). Using the TMCMC samples, the sample cumulative probability, given by Eq. (12), is shown in Figs. 12(a) and (b) for different values of the height z for the two initial nut positions $z_{init} = 0.02$ and $z_{init} = 0.1$. A relative high uncertainty in the exit time due to the parameter uncertainty is also confirmed by these Figures. These high values of uncertainty occur after the first cycle of box oscillation for height levels greater than $z = 0.14$ and $z = 0.22$ for $z_{init} = 0.02$ and $z_{init} = 0.1$, respectively. For example, for the $z_{init} = 0.02$ case, the uncertainty in the exit time of the level $z = 0.20$ ranges from approximately 3 to 10 s.

From the high uncertainty in the exit time values it can be concluded that this QoI is very sensitive to the uncertainty in the force–displacement model parameters. In contrast, a significantly lower sensitivity was observed for the fraction of time the nut remains above a certain height.

5.3. Silo discharge

The simulation of a silo-discharge [40] is characterized by the flow of particles through an orifice that is arrested if the size of the outlet is not large enough. Such a jam results in a complete and permanent halt of the flow. During the outpouring of grains, jamming occurs due to the formation of an arch at the outlet (Fig. 13).

The disks are made of the same material as before, and have a diameter of $d = 0.2$ cm. The simulation domain is a rectangle with width $W = 64d$, where d is the diameter of all the disks, and height $H = 8W$, enabling us to neglect any artifacts from boundary effects [40]. Initially $40 \times 400 = 16000$ particles are placed in a uniform rectangular lattice, almost in contact with each other (inter-particle gaps of neighboring beads are $0.05d$) and in a distance d from the bottom of the silo. These positions are randomly displaced by a distance of $0.01d$ to ensure that the initial structure will break afterwards. The outlet remains closed throughout this equilibration time (Fig. 13(a)).

We let the beads relax for 10 s in the silo after the initial drop, and subsequently open the outlet. To detect the ending of an avalanche cycle, we inspect the exit and wait until 1 s of total time elapses without a particle exiting, as proposed

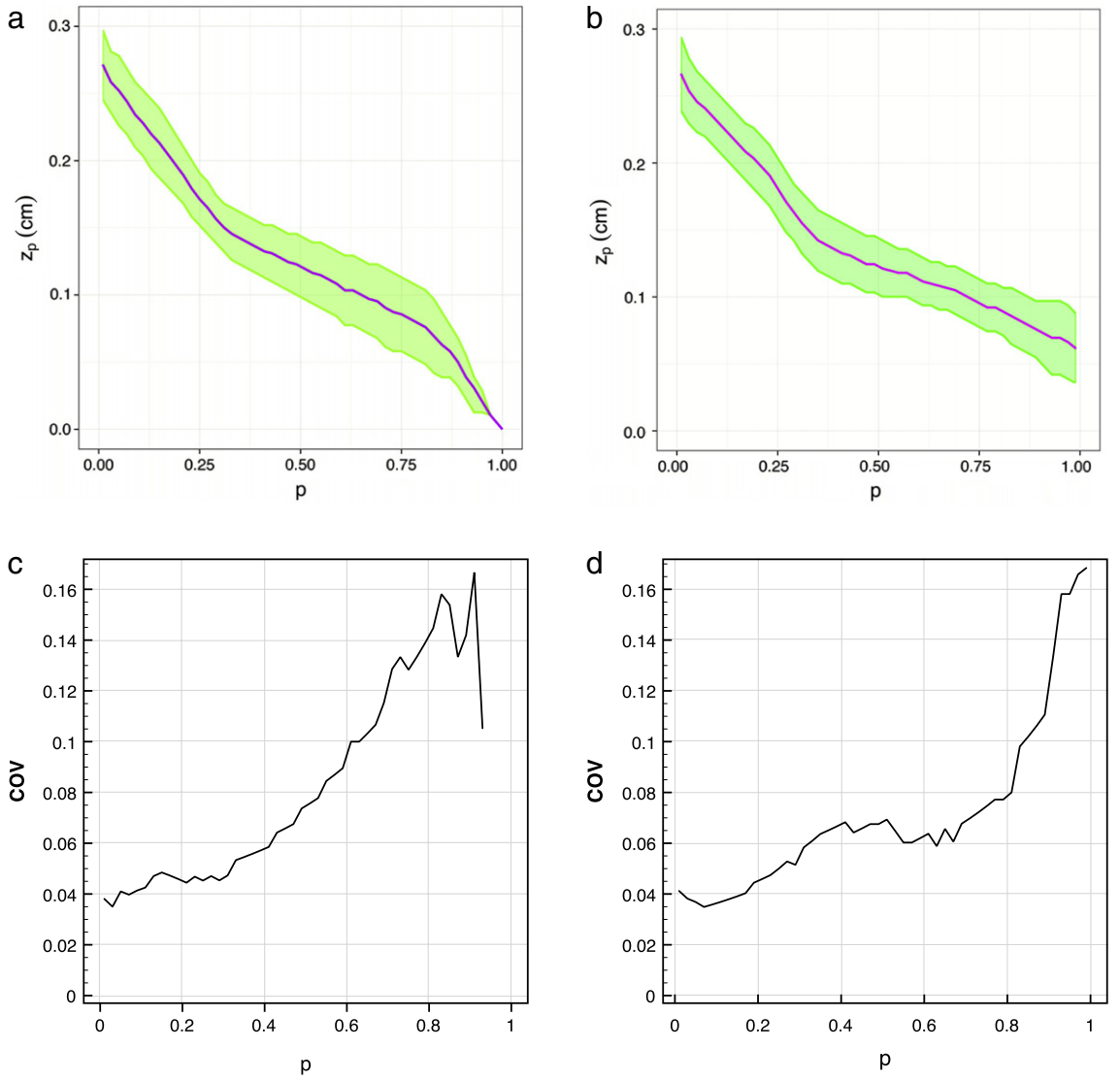

Fig. 10. Uncertainty Propagation for the first QoI z_p using M_3 and for initial nut positions $z_{init} = 0.02$ (a) and $z_{init} = 0.1$ (b). Magenta lines indicate mean values, whereas the overall uncertainty quantified as 95% quantiles is denoted with green. (c)–(d) COV with respect to plots (a) and (b) respectively. (For interpretation of the references to color in this figure legend, the reader is referred to the web version of this article.)

in [48]. Subsequently, we break the arch by extracting one of the particles forming it and placing on top of the system of beads. The simulation process is continued until the occurrence of a specified number of avalanche events. The number N_s of beads per avalanche event exiting the opening, define the size of an avalanche and are registered per avalanche event for further processing. Each propagation run consists of a campaign of 5000 avalanche events.

The simulations are performed using the model class M_3. In order to propagate the parameter uncertainty we use $N_p = 100$ samples $\theta^{(i)}, i = 1, \ldots, N_p$, from the calibration dataset obtained from the model class M_3. The selection of the 100 samples is done with weighted Poisson sampling from the 8192 posterior samples during the calibration runs with weights their posterior value. In order to minimize the computational time, we run multiple copies of the system in parallel given a parameter sample $\theta^{(i)}$ from the posterior PDF.

The QoI N_p is the avalanche size N that corresponds to fixed probability $Pr(N_s > N|\theta) = p$ of being exceeded by the simulation process. The uncertainty in the QoI $N_p(\theta)$ due to the uncertainty in the parameter vector θ as a function of the exceedance probability p is shown in Fig. 14(a). The mean predictions as well as those including the overall

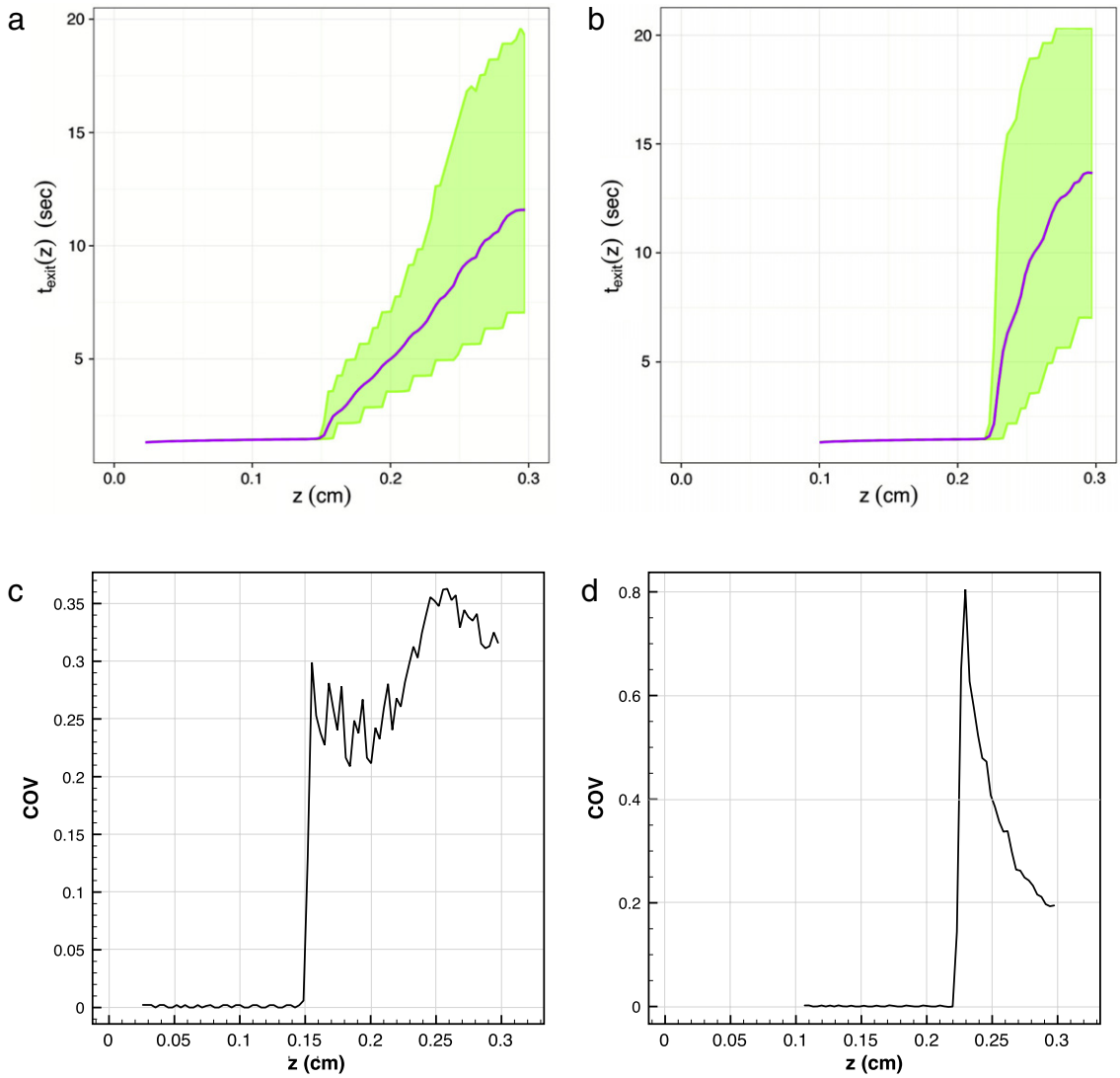

Fig. 11. Uncertainty Propagation for the second QoI t_{exit} during the mass segregation experiment using M_3 and for initial nut positions $z_{init} = 0.02$ (a) and $z_{init} = 0.1$ (b). Magenta Lines indicate mean values, whereas the overall uncertainty quantified as 5% and 95% quantiles is denoted with green. (c)–(d) COV with respect to plots (a) and (b) respectively. (For interpretation of the references to color in this figure legend, the reader is referred to the web version of this article.)

uncertainty in terms of the 5% and 95% percentile values (green lines) are shown in this figure. The 100 different curves correspond to the different sample values of θ, drawn from the posterior distribution of the model parameters. The robust estimate that takes into account the uncertainty in the parameter values is also shown in the figure. Fig. 14(b) shows the COV$(N_p(\theta))$ due to the parametric uncertainty. In particular, the robust estimate of the avalanche size with $p = 0.01$ exceedance probability is obtained from this figure to be $N_p = 45$, while the fluctuation of the avalanche size around this robust value due to parametric uncertainty ranges from $N_p(\theta) = 35$ to 52. It is observed that for high avalanche sizes, the robust estimates differ significantly from the estimates obtained from a single value of the model parameters, reinforcing the important effect of uncertainties in predictions for such avalanche sizes.

It can be seen that the highest uncertainty is observed for the larger size avalanches corresponding to relatively low exceedance probabilities, whereas the uncertainty is small in the case of small avalanches. This could be attributed to the fact that intermediate and larger avalanches entail multiple collisions between the exiting disks, therefore the effect of the parametric uncertainty is amplified, whereas single isolated events are less influenced from any collisions.

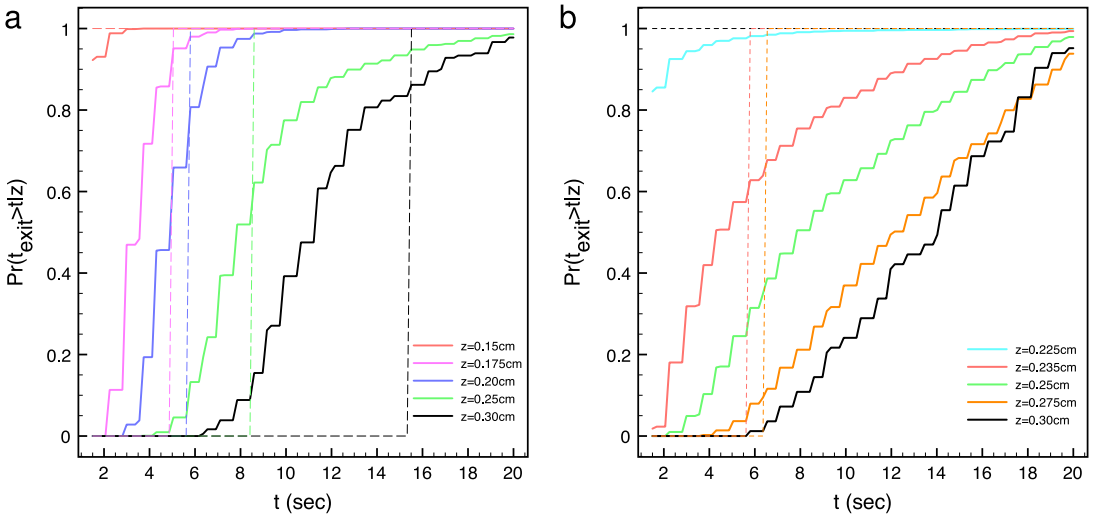

Fig. 12. Uncertainty Propagation for the third QoI during the mass segregation experiment using M_3. (a) refers to $z_{init} = 0.02$ and (b) refers to $z_{init} = 0.1$. Cumulative probabilities are depicted with solid lines whereas runs with the MAP parameters are depicted with dashed lines.

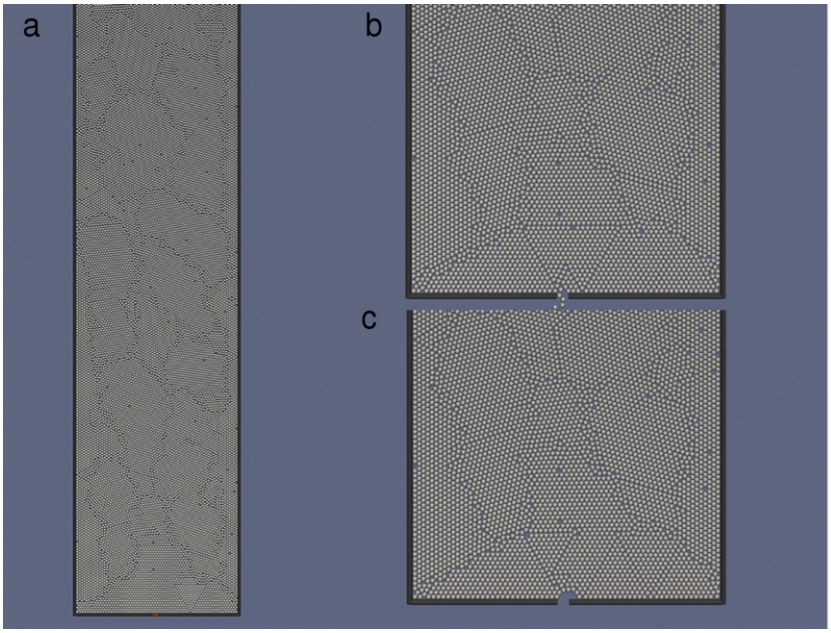

Fig. 13. Silo discharge system visualization. (a) System initialization. (b) Zoom towards the silo exit, during an avalanche. (c) Arch formation in the orifice clogging the silo. A video of the process can be seen in the Supplementary Video 2 (see Appendix A).

6. Conclusions

A Bayesian uncertainty quantification framework was been introduced to bridge the results of experiments and DEM simulations for granular flows. The framework enables a systematic parameter estimation and model selection of force–displacement models that control the interaction between particles. Upon Bayesian calibration, these models can be used to make robust model predictions for granular flows encountered in industrial applications.

In this work three Force–Displacement model classes were investigated. The first two model classes were special case of the third one which was clearly promoted as the most probable model class by the Bayesian model selection framework given the experimental data. The adequacy of the model classes was evaluated by quantifying uncertainty

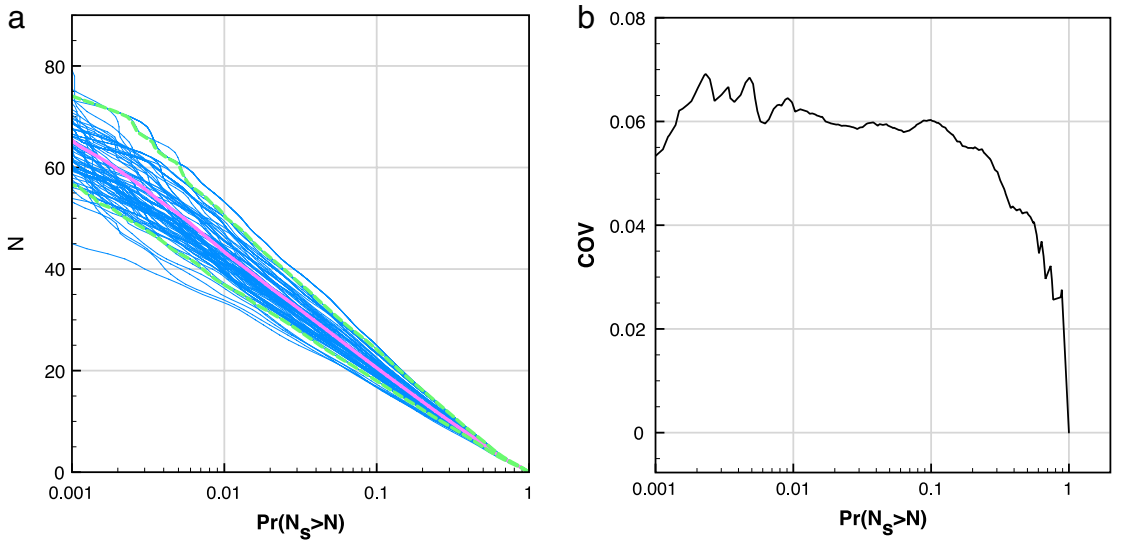

Fig. 14. (a) Uncertainty Propagation for the avalanche size N_p corresponding to fixed probability of exceedance. Results are obtained using model M_3. Magenta line indicates the robust estimate of avalanche size, blue lines indicates the estimates from the 100 different samples of the parameter values, whereas the overall uncertainty quantified as 5% and 95% quantiles is denoted with green. (b) COV of the avalanche size N_p. (For interpretation of the references to color in this figure legend, the reader is referred to the web version of this article.)

and propagating to measured coefficients of restitution. The parameter uncertainty accounted only for part of the experimental uncertainty, while the model error uncertainty was found to be important for fitting the experimental data and its uncertainty. Predictions highlighted certain weaknesses of the F–D model calibration method, as it does not cover all possible scenarios regarding initial rotational, velocity and impact angles cases that frequently occur following a multi particle collision scenario. The present findings suggest that experiments should be carried out to cover a wider parameter range and the experimental procedure should be designed carefully to reduce to the extent possible the uncertainty in the experimental data. The present Bayesian framework indicates how to systematically couple such experiments with DEM simulations to obtain improved F–D models.

The importance of robust predictions for granular flows using DEM simulations was illustrated, with two applications: the Brazil nut effect and Silo discharge for steel particles. The parametric uncertainties were propagated and their significance was demonstrated for the selected QoI for these two problems.

Current work involves the development of hierarchical F–D models for DEM simulations using Bayesian uncertainty criteria. More accurate predictions for specific applications could be achieved not by a bottom-up approach of inferring the F–D model by pairwise collisions, but by calibrating with a collective observable, such as radial distribution functions between segregating objects. Such experimental observations still remain scarce in the literature.

Acknowledgments

The fifth author would like to acknowledge funding from the Swiss NSF Program “Short International Visits”. We acknowledge computational time from the Swiss supercomputing centre CSCS under project number s448.

Appendix A. Supplementary data

Supplementary material related to this article can be found online at http://dx.doi.org/10.1016/j.cma.2014.07.017.

References

[1] P. Cundall, O. Strack, A discrete numerical model for granular assemblies, Géotechnique 29 (1) (1979) 47–65.
[2] P.W. Cleary, Large scale industrial dem modelling, Eng. Comput. 21 (2) (2004) 169–204.
[3] S.-C. Yang, S.-S. Hsiau, The simulation and experimental study of granular materials discharged from a silo with the placement of inserts, Powder Technol. 120 (3) (2001) 244–255.

[4] T.J. Goda, F. Ebert, Three-dimensional discrete element simulations in hoppers and silos, Powder Technol. 158 (1–3) (2005) 58–68.
[5] C. González-Montellano, Á. Ramírez, E. Gallego, F. Ayuga, Validation and experimental calibration of 3d discrete element models for the simulation of the discharge flow in silos, Chem. Eng. Sci. 66 (21) (2011) 5116–5126.
[6] P.A. Langston, U. Tüzün, D.M. Heyes, Discrete element simulation of granular flow in 2d and 3d hoppers: dependence of discharge rate and wall stress on particle interactions, Chem. Eng. Sci. 50 (6) (1995) 967–987.
[7] G. Marketos, C. O'Sullivan, A micromechanics-based analytical method for wave propagation through a granular material, Soil Dyn. Earthq. Eng. 45 (2013) 25–34.
[8] B. Peters, A. Dzùiugys, H. Hunsinger, L. Krebs, An approach to qualify the intensity of mixing on a forward acting grate, Chem. Eng. Sci. 60 (6) (2005) 1649–1659.
[9] G.J. Finnie, N.P. Kruyt, M. Ye, C. Zeilstra, J.A.M. Kuipers, Longitudinal and transverse mixing in rotary kilns: a discrete element method approach, Chem. Eng. Sci. 60 (15) (2005) 4083–4091.
[10] H. Kruggel-Emden, E. Simsek, S. Wirtz, V. Scherer, A comparative numerical study of particle mixing on different grate designs through the discrete element method, J. Press. Vessel Technol. 129 (4) (2007) 593–600.
[11] Y. Tsuji, T. Kawaguchi, T. Tanaka, Discrete particle simulation of two-dimensional fluidized bed, Powder Technol. 77 (1) (1993) 79–87.
[12] W. Zhong, Y. Xiong, Z. Yuan, M. Zhang, Dem simulation of gas–solid flow behaviors in spout-fluid bed, Chem. Eng. Sci. 61 (5) (2006) 1571–1584.
[13] Y. Tsuji, Multi-scale modeling of dense phase gas–particle flow, Chem. Eng. Sci. 62 (13) (2007) 3410–3418.
[14] H.P. Kuo, P.C. Knight, D.J. Parker, Y. Tsuji, M.J. Adams, J.P.K. Seville, The influence of dem simulation parameters on the particle behaviour in a v-mixer, Chem. Eng. Sci. 57 (17) (2002) 3621–3638.
[15] E. Dintwa, M. Van Zeebroeck, E. Tijskens, H. Ramon, Determination of parameters of a tangential contact force model for viscoelastic spheroids (fruits) using a rheometer device, Biosystems Eng. 91 (3) (2005) 321–327.
[16] C.J. Coetzee, D.N.J. Els, Calibration of discrete element parameters and the modelling of silo discharge and bucket filling, Comput. Electron. Agric. 65 (2) (2009) 198–212.
[17] E. Alizadeh, F. Bertrand, J. Chaouki, Development of a granular normal contact force model based on a non-newtonian liquid filled dashpot, Powder Technol. 237 (2013) 202–212.
[18] F.P. Di Maio, A. Di Renzo, Modelling particle contacts in distinct element simulations: linear and non-linear approach, Chem. Eng. Res. Des. 83 (11) (2005) 1287–1297.
[19] H. Kruggel-Emden, S. Wirtz, V. Scherer, A study on tangential force laws applicable to the discrete element method (dem) for materials with viscoelastic or plastic behavior, Chem. Eng. Sci. 63 (6) (2008) 1523–1541.
[20] J.L. Beck, K.-V. Yuen, Model selection using response measurements: Bayesian probabilistic approach, J. Eng. Mech. 130 (2) (2004) 192–203.
[21] J.T. Oden, A. Hawkins, S. Prudhomme, General diffuse interface theories and an approach to predictive tumor growth modeling, Math. Models Methods Appl. Sci. 20 (3) (2010) 477–517.
[22] K.-V. Yuen, Bayesian Methods for Structural Dynamics and Civil Engineering, Wiley-Vch Verlag, 2010.
[23] J.L. Beck, S.K. Au, Bayesian updating of structural models and reliability using Markov chain monte carlo simulation, J. Eng. Mech. 128 (4) (2002) 380–391.
[24] X. Ma, N. Zabaras, A stochastic mixed finite element heterogeneous multiscale method for flow in porous media, J. Comput. Phys. 230 (12) (2011) 4696–4722.
[25] S.H. Cheung, T.A. Oliver, E.E. Prudencio, S. Prudhomme, R.D. Moser, Bayesian uncertainty analysis with applications to turbulence modeling, Rel. Eng. Sys. Saf. 96 (9) (2011) 1137–1149.
[26] P.M. Congedo, P. Colonna, C. Corre, J.A.S. Witteveen, G. Iaccarino, Backward uncertainty propagation method in flow problems: application to the prediction of rarefaction shock waves, Comp. Meth. Appl. Sci. Eng. 213–216 (2012) 314–326.
[27] P.L. Garrido, J. Marro, H.J. Herrmann, 3rd Granada Lectures in Computational Physics, vol. 448, Springer, Berlin, Heidelberg, 1995, pp. 67–114 (Chapter 2).
[28] J. Ching, Y.C. Chen, Transitional Markov chain monte carlo method for Bayesian model updating, model class selection, and model averaging, J. Eng. Mech. 133 (7) (2007) 816–832.
[29] P. Angelikopoulos, C. Papadimitriou, P. Koumoutsakos, Bayesian uncertainty quantification and propagation in molecular dynamics simulations: a high performance computing framework, J. Chem. Phys. 137 (14) (2012) 144103.
[30] P.E. Hadjidoukas, E. Lappas, V.V. Dimakopoulos, A runtime library for platform-independent task parallelism, in: 20th Euromicro International Conference on Parallel, Distributed and Network-Based Processing (PDP), IEEE Computer Society, Munich, Germany, 2012, pp. 229–236.
[31] T. Pöschel, T. Schwager, Computational Granular Dynamics—Models and Algorithms, Springer-Verlag, New York, 2005.
[32] H. Kruggel-Emden, M. Sturm, S. Wirtz, V. Scherer, Selection of an appropriate time integration scheme for the discrete element method (dem), Comput. Chem. Eng. 32 (10) (2008) 2263–2279.
[33] H. Hertz, Ueber die berührung fester elastischer körper, J. Reine Angew. Math. 1882 (1882) 156.
[34] S. Timoshenko, J.N. Goodier, Theory of elasticity, in: Engineering Societies Monographs, McGraw-Hill, New York, 1969.
[35] H. Kruggel-Emden, F. Stepanek, A. Munjiza, Performance of integration schemes in discrete element simulations of particle systems involving consecutive contacts, Comput. Chem. Eng. 35 (10) (2011) 2152–2157.
[36] Y. Tsuji, T. Tanaka, T. Ishida, Lagrangian numerical simulation of plug flow of cohesionless particles in a horizontal pipe, Powder Technol. 71 (3) (1992) 239–250.
[37] G. Kuwabara, K. Kono, Restitution coefficient in a collision between two spheres, Japan. J. Appl. Phys. 26 (1987) 1230–1233. Part 1, No. 8.
[38] N.V. Brilliantov, F. Spahn, J.-M. Hertzsch, T. Pöschel, Model for collisions in granular gases, Phys. Rev. E 53 (1996) 5382–5392.
[39] L. Brendel, S. Dippel, Lasting contacts in molecular dynamics simulations, in: Physics of Dry Granular Media, Kluwer Academic Publishers, 1998, pp. 31–33.

[40] D. Hirshfeld, D. Rapaport, Granular flow from a silo: discrete-particle simulations in three dimensions, Eur. Phys. J. E 4 (2) (2001) 193–199.
[41] H. Jeffreys, Theory of Probability, third ed., Oxford University Press, USA, 1961.
[42] E. Simoen, C. Papadimitriou, G. Lombaert, On prediction error correlation in Bayesian model updating, J. Sound Vib. 332 (18) (2013) 4136–4152.
[43] A. Doucet, N. De Freitas, N. Gordon, Sequential Monte Carlo Methods in Practice, Springer, 2001.
[44] C. Papadimitriou, J.L. Beck, L.S. Katafygiotis, Updating robust reliability using structural test data, Prob. Eng. Mech. 16 (2) (2001) 103–113.
[45] A. Taflanidis, J.L. Beck, Prior and posterior robust stochastic predictions for dynamical systems using probability logic, Int. J. Unc. Qu. 3 (4) (2013) 271–288.
[46] H. Dong, M.H. Moys, Experimental study of oblique impacts with initial spin, Powder Technol. 161 (1) (2006) 22–31.
[47] T. Schwager, V. Becker, T. Pöschel, Coefficient of tangential restitution for viscoelastic spheres, Eur. Phys. J. E 27 (1) (2008) 107–114.
[48] I. Zuriguel, A. Garcimartín, D. Maza, L. Pugnaloni, J. Pastor, Jamming during the discharge of granular matter from a silo, Phys. Rev. E 71 (2005) 051303.